Article

Experimental Analysis of Acoustic Spectra for Leading/Trailing-Edge Serrated Blades in Cascade Configuration

Andrei-George Totu [1,2,*] **, Marius Deaconu** [2] **, Laurențiu Cristea** [2] **, Alina Bogoi** [1,2] **, Daniel-Eugeniu Crunțeanu** [1] **and Grigore Cican** [1,2]

1   Faculty of Aerospace Engineering, National University of Science and Technology Politehnica Bucharest, 1-7 Polizu Street, 1, 011061 Bucharest, Romania; daniel.crunteanu@upb.ro (D.-E.C.); grigore.cican@comoti.ro (G.C.)
2   National Research and Development Institute for Gas Turbines—COMOTI, 220D Iuliu Maniu, 061126 București, Romania; marius.deaconu@comoti.ro (M.D.); laurentiu.cristea@comoti.ro (L.C.)
*   Correspondence: andrei.totu@comoti.ro

Abstract: This study aims to highlight the noise reduction achieved through the integration of serrated blades on the leading and trailing edges within a small-scale cascade configuration relevant to turbomachinery contexts. Experiments were conducted using a newly developed 3D-printed test bench, enabling both acoustic and aerodynamic measurements. Turbulence was generated using a rectangular grid positioned at two axial locations. Non-dimensional spectra were computed and compared with experimental data, showing good agreement over a wide frequency range. Significant noise reduction was observed in the 1000–3000 Hz band, despite the lack of optimization of turbulence and serration parameters. Leading-edge serrations were found to be effective at lower frequencies in the axial direction and at higher frequencies laterally. In contrast, trailing-edge serrations had a minimal impact above 3500 Hz, performing worse than the reference condition across a large frequency range. Nevertheless, for this initial iteration at a small scale, overall sound pressure level reductions of up to 1 dB were achieved with trailing-edge serrations and up to 1.5 dB with leading-edge serrations, underscoring their potential for noise mitigation in relevant applications.

Keywords: turbomachinery; serrations; cascade; interaction noise

1. Introduction

Studying serrated blades and their impact on noise reduction has been a topic of interest in the field of aerodynamics and acoustics (since the 1950s [1]) due to noise, efficiency, and environmental impact. Serrated blades, with serrations on either the leading edge or trailing edge, have shown potential in reducing noise generated by aerodynamic components such as fans [2–4], turbines [5,6], and propellers [7,8]. The serrations can help in breaking up the airflow and reducing turbulence (which is the main source for mixing noise [9]), leading to quieter operation.

Serrated blades can enhance the overall efficiency of aerodynamic components by improving airfoil performance. These serrations modify the flow characteristics, resulting in better lift-to-drag ratios and reduced energy losses [10]. More advanced approaches, such as permeable regions (metamaterials), have also demonstrated promising potential [11]. Noise pollution generated by aerodynamic components poses a significant challenge, particularly in urban and residential areas [12,13]. Investigating serrated blades for noise reduction offers the potential for developing quieter and more environmentally sustainable technologies [14].

Researching serrated blades provides an opportunity for innovation and optimization in aerodynamic design. By understanding the impact of serrations on noise reduction, engineers can develop more efficient and quieter aerodynamic components for various applications. Overall, studying serrated blades and their impact on noise reduction is essential for advancing aerodynamic technologies, improving efficiency, reducing noise pollution, and promoting sustainable practices in the field of aerospace engineering and beyond.

Concerning the behavior of blades in isolated versus cascade configurations, Lewis et al. [15] provide a comprehensive overview of the mathematical models developed over time, demonstrating how the equations describing the interactions and propagation within the flow channel result in a computed spectrum that closely approximates the experimental measurements. At the same time, general formulas for both the simplest spectra (flat plate, Amiet), both isolated [10] and in cascade configuration [15,16], have been identified in the literature, as well as the jet mixing noise [12,17,18]. A well-developed computational workflow, identified in the literature, is shown in Figure 1.
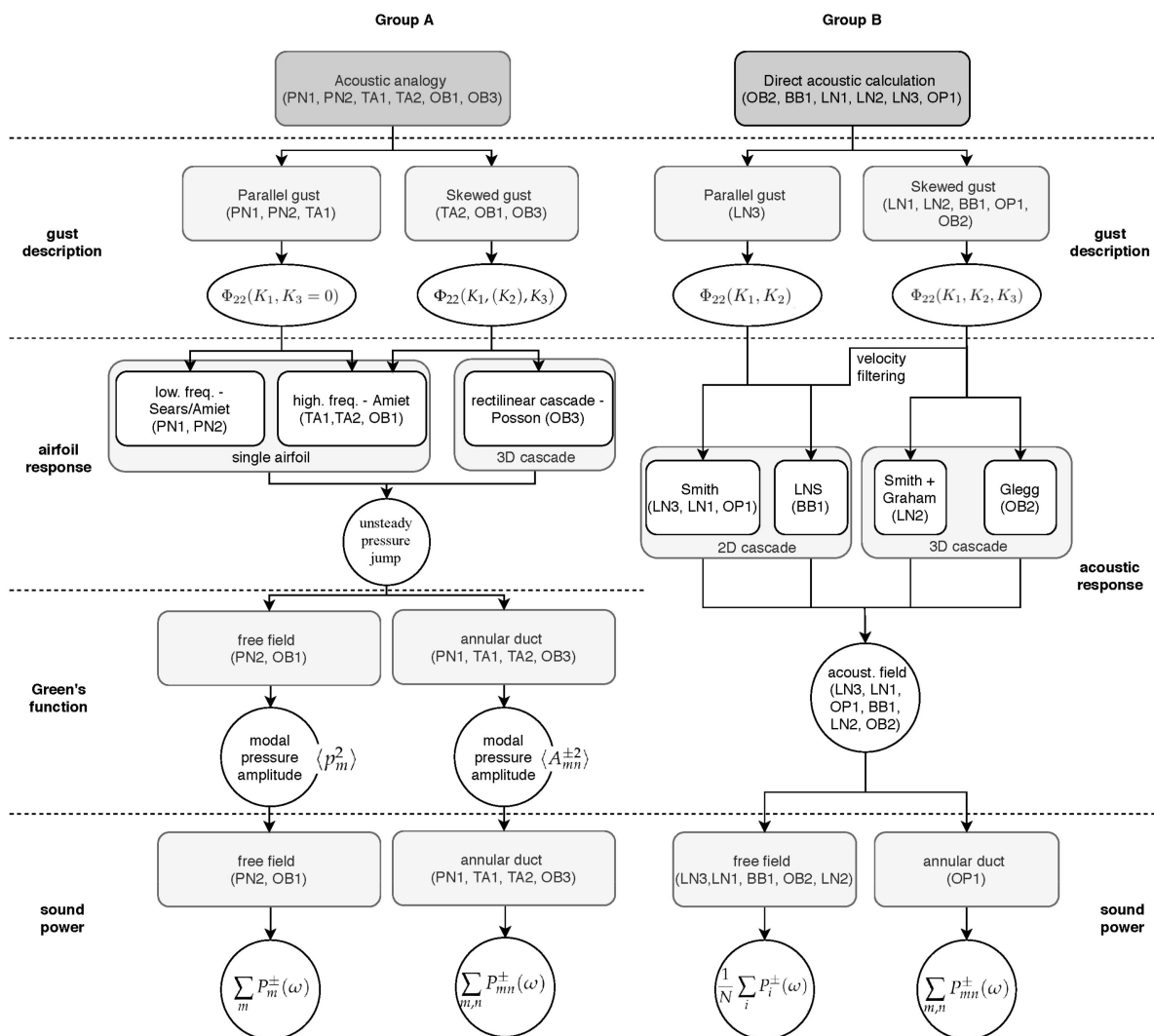

Figure 1. Example of computational workflow applicable to both the isolated airfoil and cascade configurations: Group A—Methods based on the acoustic analogy; Group B—direct calculation of the acoustic pressure response of the cascade of blades without requiring a source term [19].

Turbulence is a phenomenon characterized by irregular and chaotic motions in a fluid, caused by the complex interaction between different fluid layers [1,15,20,21]. These motions are often unpredictable and usually develop under fast or disturbed flow conditions, such as in aviation turbomachinery. The importance of turbulence in engineering and science is crucial as it has a significant impact on the performance and efficiency of various systems and devices [2,18,22]. In the case of aviation gas turbines, turbulence can lead to increased energy losses and decreased engine efficiency. It is therefore essential to understand the behavior of turbulence and to develop effective methods to control and predict it. In addition, turbulence also plays an important role in other fields, such as in

fluid transportation, meteorology, oceanography, and even in wind energy production. Understanding and correctly modeling turbulence phenomena are essential for improving system performance, reducing energy losses, and optimizing technological processes [23–25].

Mathematical models for turbulence are essential for describing and predicting the behavior of turbulent fluids in various contexts, such as aerodynamics and hydrodynamics. Turbulence is a complex, chaotic phenomenon that cannot be directly predicted from the fundamental equations of fluid mechanics, namely the Navier–Stokes equations. Different types of turbulence exist, which can be classified based on the nature of the fluid flow and the intensity of the turbulent motion. The most common types of turbulence are isotropic turbulence (characterized by the same intensity of turbulent motion in all directions) [10,26], two-dimensional turbulence (the flow is only in two dimensions, which simplifies the mathematical analysis) [26,27], boundary layer turbulence (occurs near solid surfaces, where turbulent motions are strongly influenced by the adhesion of the fluid to the surface) [11,15,22], and high-velocity turbulence (occurs in high-velocity flows, such as those near airplanes or ships) [13,17,18]. A comparative analysis of various turbulence models and scales is conducted, focusing on the accuracy of their predictions when compared to experimental data acquired under real-world conditions.

To physically replicate turbulence in gas turbine engine stages, mathematical models and computational simulations are required to accurately simulate fluid dynamics under well-defined conditions. These simulations may involve detailed analysis of the fluid flow, pressure, and temperature within the engine, as well as the interactions between different engine components. Experimental tests may also be conducted in wind tunnels or other test environments to observe turbulence behavior under real-world conditions. It is important to take into account factors such as engine geometry, air flow velocity, and operating conditions to obtain the most accurate recreation of flow conditions. The selection of a mathematical model depends on the specific objectives of the study and the inherent complexity of turbulence behavior in the given application. Models can also be evaluated based on several criteria, including predictive accuracy, generalization capacity, computational efficiency, and their ability to accommodate the boundary conditions specific to the problem at hand [15,28,29].

In gas turbine and turbofan engines, turbulence is a ubiquitous phenomenon that significantly influences the performance and efficiency of these systems. The turbulence scale is typically determined through mathematical models and computational simulations, which are used to analyze fluid behavior. It is defined as the ratio of inertial forces to viscous forces and serves as an indicator of the turbulence intensity within a given system. Additionally, the turbulence scale can be interpreted as the characteristic length associated with turbulence in a fluid medium, defined as the distance traveled by a fluid particle between two successive turbulent interactions. In real-life experimentation, the following equipment can be used to measure the parameters describing turbulence: anemometers (for measuring fluid velocity at different points to assess the degree of turbulence), usually hot wire anemometers or probes (for measuring fluid velocity and temperature fluctuations) [2,10,30,31], Pitot tubes (for measuring fluid pressure and velocity) [14], pressure sensors (to measure pressure variations in the fluid stream or on surface) [31,32], and also high-speed cameras integrated in a PIV ("Particle Image Velocimetry") setup [27,33] (to visualize and record the turbulence pattern created due to fast and dispersed fluid flow). A combination of these tools is essential for defining the levels of velocity and pressure fluctuations (as in [34]) in the fluid flow (n.b. u' and p') [22], the turbulent kinetic energy and the turbulent kinetic energy dissipation rate (K and also ε), the rate at which fluctuations in the fluid flow occur (f) [15], and the (integral length scale of turbulent structures in the fluid flow (Λ) [15,22,35]:

$$
\begin{aligned}
TI &= \sqrt{\frac{\overline{u'^2}}{U_0^2}} \\
\overline{u'^2} &= \int_{-\infty}^{+\infty} S_{uu}(f)\,df \\
\Lambda &= \frac{U_0 S_{uu}(f=0)}{2\overline{u'^2}}
\end{aligned}
\tag{1}
$$

where TI is the turbulent intensity and S_{uu} is the longitudinal turbulent velocity spectra. To artificially generate turbulence in an experimental setup, different methods can be used, such

as orifice plates (circular grids) [36–38], grids [10,20,22], rotating vanes or active grids [39], rods [40–42], or pulsed air jets [43]. These devices can be used to disturb fluid flow and create turbulence in a controlled manner. Numerical simulations are also used to model and induce artificial turbulence in experimental setups. Consideration of setup geometry, airflow velocity, and operating parameters is crucial for obtaining reliable and reproducible results.

Turbulence scales are theoretical concepts that describe the transfer of energy and viscosity between different turbulence scales in a fluid medium. There are several models of turbulence scales, each with their own characteristics and relevant parameters. A brief description of some turbulence scale models and their associated parameters follows:

- The von Kármán turbulence scale [10,22,35,44–46] (this model focuses on the energy transfer between different turbulence scales and how the characteristic length scales are related to the energy cascade process). This scale provides insight into how large-scale turbulent flows induce fluctuating pressure fields that propagate as sound. Energy transfer across different scales leads to vortex shedding, which can produce tonal noise due to periodic pressure fluctuations at distinct frequencies. This process generates a low-pressure region, where noise is produced as the airflow transitions from laminar to turbulent. In applications such as aircraft wings, propeller blades, or helicopter blades, this results in a specific "whooshing" sound due to the interaction of airflows around the wings.
- The Liepmann turbulence scale [10,35,45] (this model deals with the interaction between turbulence and viscosity in a fluid medium, typically specific to turbulent boundary layer trailing edge noise). The interaction between turbulence and viscosity at this scale affects how sound is generated at the trailing edge of blades. As the turbulent layer of air forms due to irregular fluid motion, it produces a distinct sound when it breaks up at the downwind edge, contributing to the overall noise emitted by the blades. When the turbulent boundary layer interacts with the blade, it generates oscillating pressure variations that resemble a dipole pattern of sound radiation.
- The Taylor turbulence scale [47,48] (this model focuses on the transfer of kinetic energy between different turbulence scales, e.g., an intermediate length scale at which fluid viscosity significantly affects the dynamics of turbulent eddies in the flow). As the blade moves into a turbulent layer of air, the energy transfer can cause scattering at the leading edge, radiating noise. This noise can vary widely in frequency, contributing to the overall roar associated with high-velocity flows around the airfoil.
- The Obukhov–Corrsin turbulence scale [49,50] (this model deals with energy and viscosity transfer in turbulence, also taking into account thermal gradient effects). Inflows with thermal gradients create density fluctuations that affect the turbulence around the blunt trailing edge of the blade. Airflow past the blade tip generates turbulent vortices, producing a distinctive type of noise, typically described as a deep rumble linked to energy dissipation within the turbulent flow.
- The Kolmogorov turbulence scale [47] (this model focuses on the smallest turbulence scale, known as the Kolmogorov scale, which describes the behavior of turbulence at the molecular level). At the smallest scales, the turbulence characterized by the Kolmogorov scale is crucial for understanding the fine details of sound generation. As the angle of attack increases, airflow becomes separated from the blade, creating zones of turbulence that generate low-level noise. This can manifest as a soft, continuous roar, typical in conditions where blades operate near their stall limits.
- Other scales, Batchelor (1959, [50]), Ozmidov (1965, [49]), Monin-Obukhov [51], Corrsin (1970, [52]), Kraichnan [45], Kaimal and Davenport [53]—for a larger scale application, etc.

In the von Kármán model, the characteristic length scale of turbulence refers to the typical size of turbulent structures within a fluid medium, such as eddies. The turbulence energy in the von Kármán spectrum is typically expressed as spectral density [44], with units of energy per unit frequency or wave number. These units may vary depending on the context of the turbulence spectral analysis. Turbulence spectra can be computed using

specialized functions for spectral signal analysis to visualize the distribution of turbulence energy as a function of frequency or wavenumber, employing the von Kármán interpolation formula, and the following equation can be used [46]:

$$E(k) = \frac{55}{9\sqrt{\pi}} \frac{\Gamma\left(\frac{5}{6}\right)\overline{u'^2}}{\Gamma\left(\frac{1}{3}\right)k_e} \frac{\left(\frac{k}{k_e}\right)^4}{\left[1 + \left(\frac{k}{k_e}\right)^2\right]^{\frac{17}{6}}} \tag{2}$$

where k is the magnitude of the vector wave number, $\Gamma()$ refers to the Gamma function and $k_e = \frac{\sqrt{\pi}}{\Lambda_f} \frac{\Gamma\left(\frac{5}{6}\right)}{\Gamma\left(\frac{1}{3}\right)}$ is the wavenumber scale of the largest eddies.

The von Kármán longitudinal one-dimensional turbulence spectrum, obtained by integrating the energy spectrum, is given by

$$\Phi_{uu}(k_x) = \int_{-\infty}^{\infty} \int_{-\infty}^{\infty} \frac{E(k)}{4\pi k^2} \left(1 - \frac{k_x^2}{k^2}\right) dk_z dk_y = \frac{2}{\sqrt{\pi}} \frac{\Gamma\left(\frac{5}{6}\right)\overline{u'^2}}{\Gamma\left(\frac{1}{3}\right)k_e} \left[1 + \left(\frac{k_x}{k_e}\right)^2\right]^{-\frac{5}{6}} \tag{3}$$

The von Kármán model is also the basis of many mathematical models that evaluate acoustic pressure spectra, such as the TNO-Blake model [35] mentioned by Suresh et al. [54] used to determine the surface pressure spectrum beneath a turbulent boundary layer near the trailing edge of an airfoil. There are also several variations of this formulation, such as the von Kármán–Pao energy spectrum [44].

2. Materials and Methods

The experimental setup was coupled to a 9800 Pa, 7.5 kW centrifugal fan (SODECA CA-172-2T-10 IE3) and placed in the anechoic chamber designed and executed according to ISO3745 [33] requirements, with a volume of 1200 m^3, 15 × 10 × 8 m and with a wall absorption coefficient of 99%, in a frequency range of 150 Hz up to 20,000 Hz. The compressor was placed outside the anechoic chamber; it was connected to the flexible 20 m-long tubing. The test section was placed diagonally so that the air tubing was curved as little as possible. Two class 1 sound level meters (Acoem Fusion, Limonest, France) were placed within a radius of 1 m, the first roughly in the direction of flow (at ~10 degrees to the longitudinal axis of the nozzle) and the second at 90 degrees to the axis (Figure 2). Raw noise signals were recorded at an acquisition rate of 50 ks/s. Similar, but much more elaborate setups, which capture the behavior of blades in a cascade configuration include those in [22,55]. Corrections for the spectra measured at 90 degrees, initially determined with the longitudinal propagation correlations, were identified in [56] for Mach numbers of 0.5 and a cold jet. Reflections within the cascade, compared to the isolated airfoil, should be assessed similarly to the models proposed in [57].
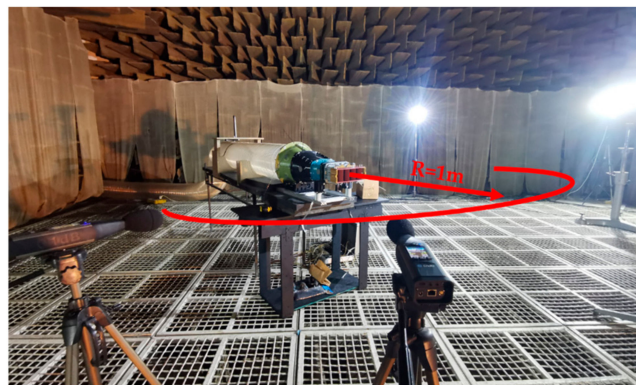

Figure 2. Test setup.

As experimental configurations, a combination of printed vanes and grids was performed to demonstrate the noise reduction capabilities of such vanes (with serrations—here,

rounded triangular cutouts with an amplitude equal to 20% of the chord length). Figure 3 shows the test configurations placed at the nozzle outlet. The position of the grids in the configurations is also shown in Figure 4 (the first at the converging channel inlet, approx. 600 mm upstream of the outlet, and the second 350 mm downstream of the converging inlet). In order to correlate theoretical spectra with those obtained experimentally, it is necessary to know the flow velocity. For this purpose, a Type L Pitot tube from Kimo (Figure 5—left) was used and the measurements were performed considering the blade arrangement in the cascade (setting angle). Several measurements along the blade length were performed at the cascade outlet and were averaged for each of the 5 cases (Figure 5—right, U_0 parameter).
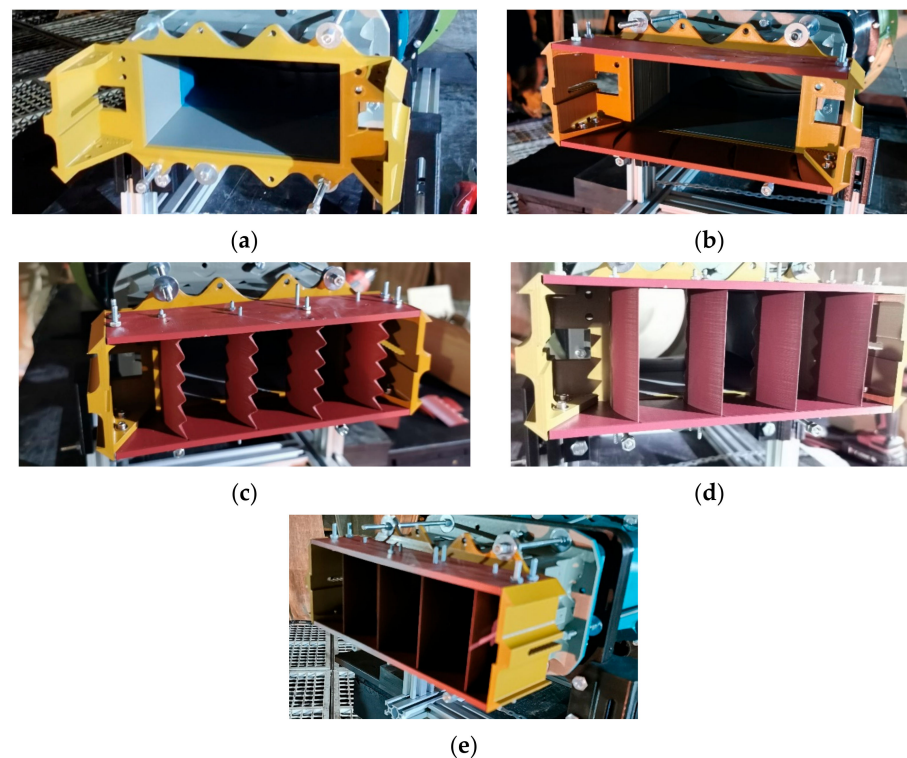
(**a**)

(**b**)

(**c**)

(**d**)

(**e**)

Figure 3. Tested configurations: (**a**) Simple outlet; (**b**) Outlet + top/bottom plates; (**c**) Trailing-edge serrations; (**d**) Leading-edge serrations; (**e**) Reference cascade (straight leading edge).
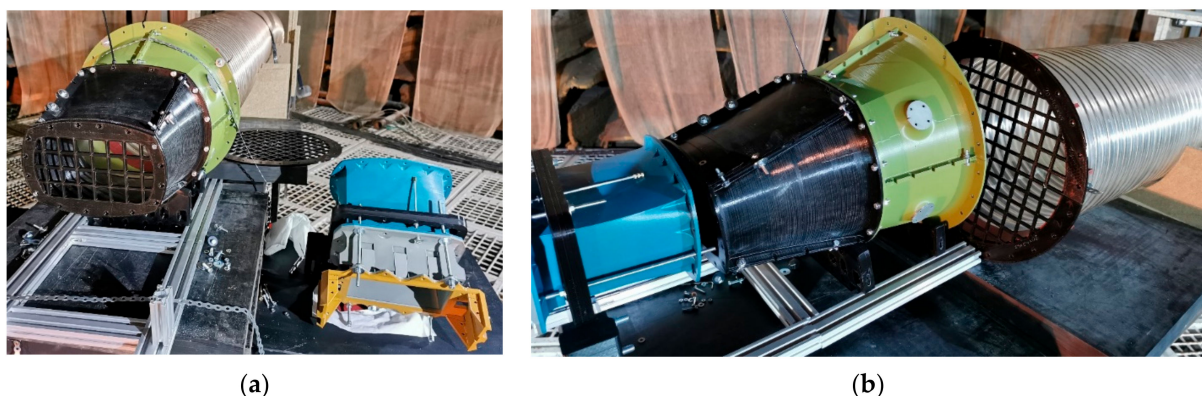
(**a**)

(**b**)

Figure 4. Turbulence grid placement: (**a**) 2nd position (closer to outlet section); (**b**) 1st position (closer to inlet section).

The raw signals were processed in dBFa (ACOEM company, Limonest, France) software where a frequency-domain FFT analysis was performed in the 10–20,000 Hz frequency range with a spectral resolution of 1.25 Hz, Hanning-type filtering, and 50% overlap between data blocks, and RMS values were calculated.
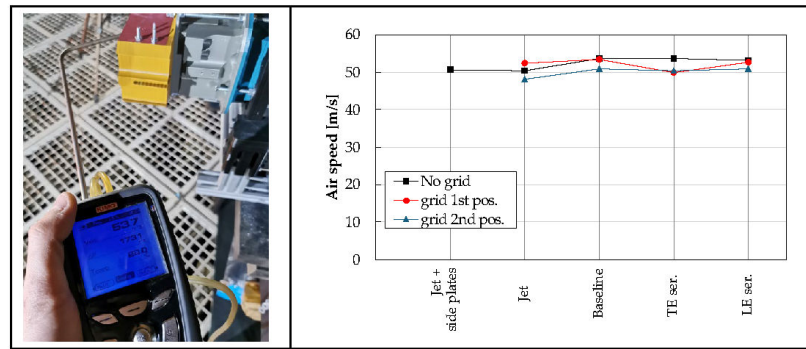
Figure 5. Flow speed measurements at the exit of the vane section.

3. Results

The preliminary tests were divided into three series. In the first series, the aim was to highlight the self-noise of the blades as well as the noise generated exclusively by the jet (with and without the plates supporting the blades). Figure 6 shows the results of this first campaign.
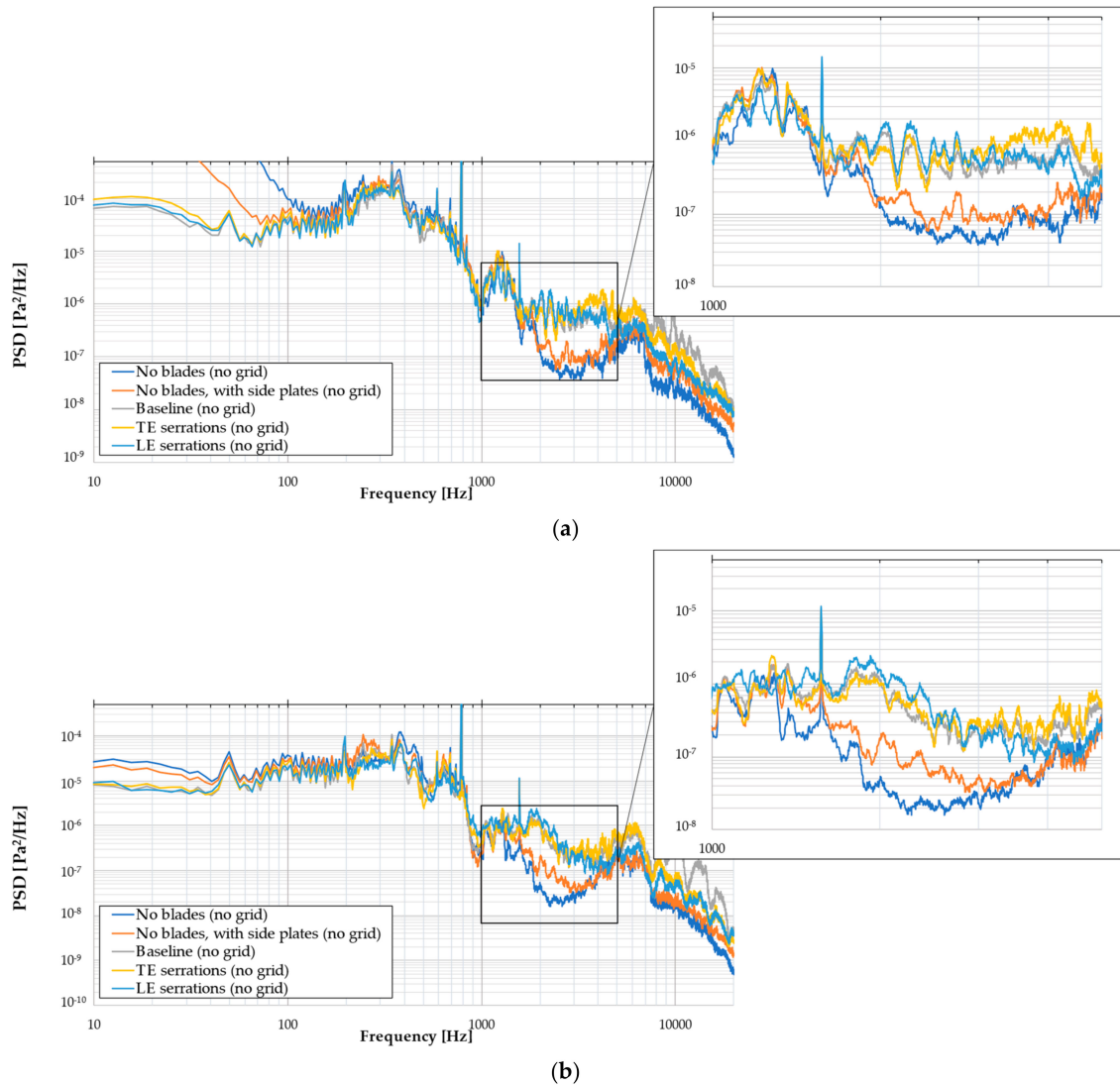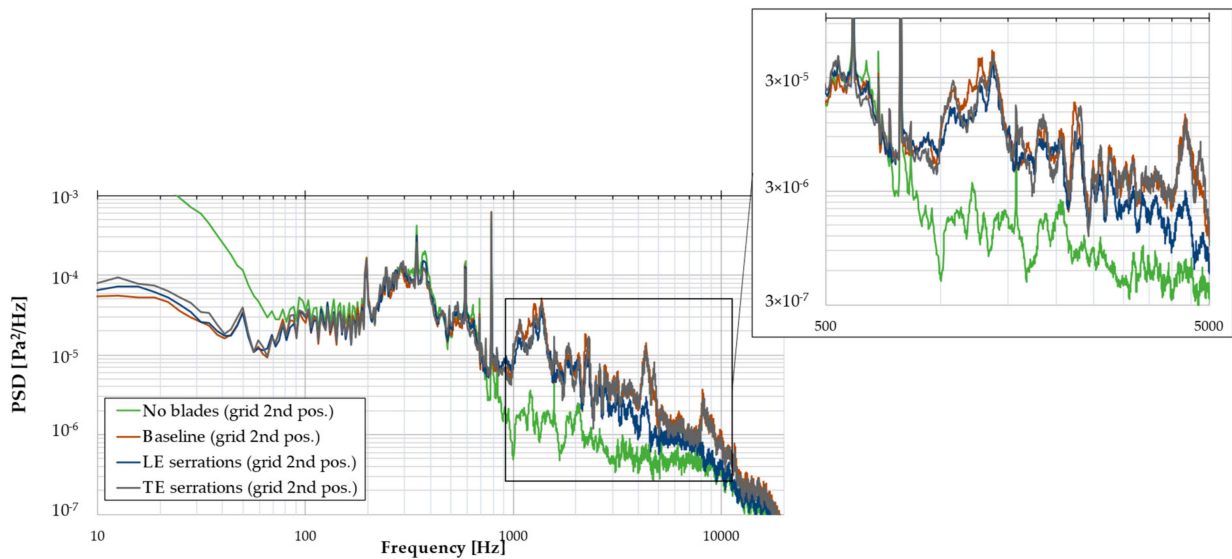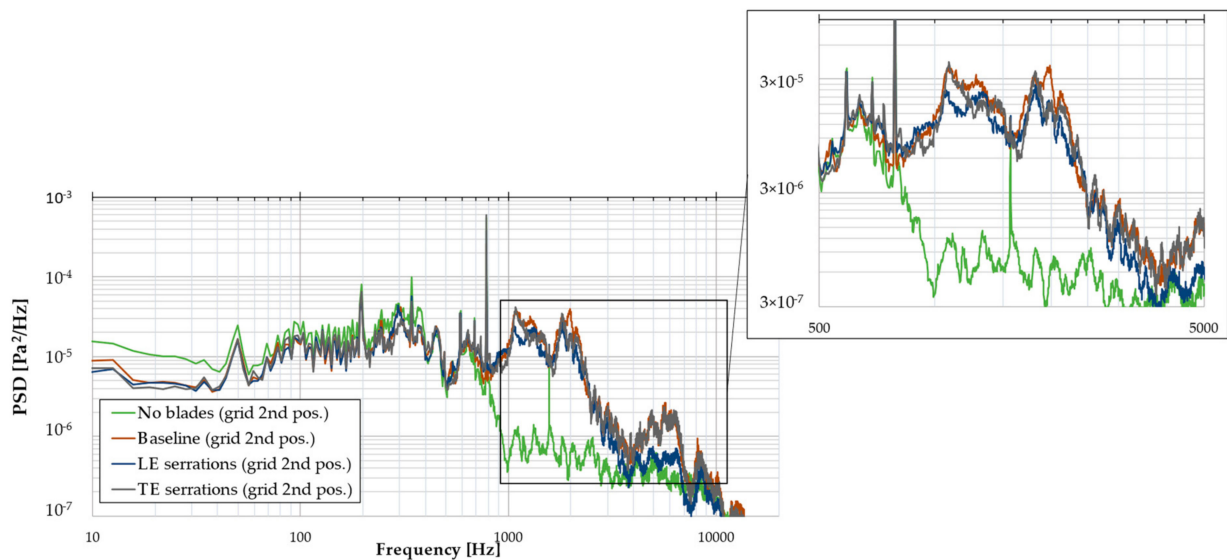

(**a**)

(**b**)

Figure 6. Vane self-noise: (**a**) 0–20 kHz spectrum + detail on the frequency range of interest (multiples of BPF)—Microphone 1 (10 degrees to the longitudinal axis); (**b**) 0–20 kHz spectrum + detail on the frequency range of interest (multiples of BPF)—Microphone 2 (⊥ to the longitudinal axis).

It can be seen that the spectra in Figure 6 have quite a lot of undesired noise, with the predominant noise (at ~786 Hz and first harmonic) coming from the impeller, propagating on the air duct. The jet exiting the nozzle also produces noise around 1000 Hz, with the interaction noise being broadband (the noise reduction mechanism being best identified above 1500 Hz). Other peaks occurring at higher frequencies (above but not only 5 kHz) may originate from weak sealing.

The second series of tests was based on placing a grid (20 mm × 20 mm and 4.5 mm thick) in front of the vane sector (~300 mm). In addition to the jet noise, a reduction in the overall sound pressure level of approximately 1.5 dB was observed for the LE-serrated vanes compared to normal vanes (with straight LE). For blades with TE serrations, less than 1 dB reduction in overall noise was recorded (Figure 7).

(**a**)

(**b**)

Figure 7. Interaction noise (turbulence grid at 2nd position): (**a**) 0–20 kHz spectrum + detail on the frequency range of interest (multiples of BPF)—Microphone 1 (10 degrees to the longitudinal axis); (**b**) 0–20 kHz spectrum + detail on the frequency range of interest (multiples of BPF)—Microphone 2 (⊥ to the longitudinal axis).

A quantitative analysis for the two treatments could have been carried out using the "log law" determined by Paruchuri [22] which uses acoustic power levels, the dependence being mainly on the Strouhal number, or a similar power law as in [2].

As for analyzing how the differences between turbulence scales influence the characteristics of the generated noise, the parameter Λ can be varied and using the relations proposed in [45] the spectra in Figure 8 are obtained. The formulation used is expressed in the form of energy spectra and normalized to the parameter K (kinetic energy). Another Gaussian shape function for synthetic eddies was identified in [44].

$$
\begin{aligned}
E_{\text{Gauss}}(k) &= \frac{2}{\pi^2} K\lambda^4 k^3 \exp\left(-\frac{\lambda^2 k^2}{\pi}\right) \\
E_{Liepmann}(k) &= \frac{16}{3\pi} K\lambda^5 \frac{k^4}{(1+\lambda^2 k^2)^3} \\
E_{vK}(k) &= \frac{110}{27\pi} K\varsigma^4 \frac{k^4}{(1+\varsigma^2 k^2)^{\frac{17}{6}}}
\end{aligned}
\tag{4}
$$

where $\varsigma = \frac{\Gamma\left(\frac{1}{3}\right)}{\sqrt{\pi}\Gamma\left(\frac{5}{6}\right)}\lambda$ and λ is the integral length scale.
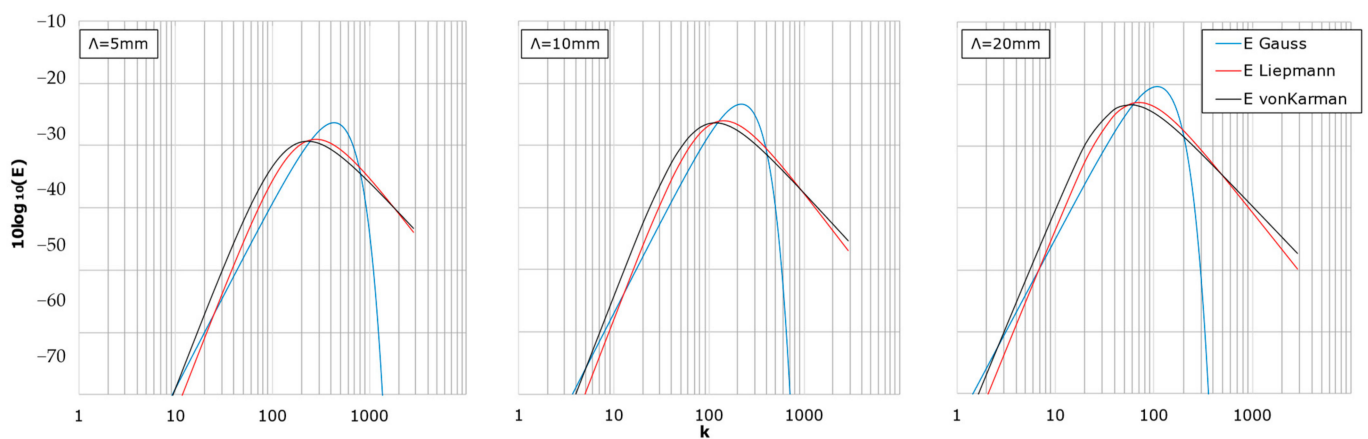

**Figure 8.** Various computed energy spectra for different Λ.

From Figure 8, it is clear that unlike the established von Kármán and Liepmann formulations, which reproduce the $-5/3$ slope (Kolmogrov's law) in the second half of the spectrum (inertial subrange) very well, the energy loss captured by the Gaussian spectrum at the universal subrange is compensated by a higher peak, so that "by integrating the subgraph area" approximately the same target value of the kinetic energy is reached [45].

Figure 9 presents the formulas for the von Kármán and Liepmann spectra alongside the acoustic spectra recorded at 1 m from the convergent nozzle output, as shown in Figure 2. Both the theoretical and recorded acoustic spectra values were normalized to a [0, 1] range. This normalization converts the values into dimensionless quantities, enabling comparison between different methods and physical phenomena, and subsequently with the measured data. However, a challenge arises when these spectra need to be compared with a value derived from power. The graphs may look similar, but they are not, neither in values nor in understanding the phenomenon. For this purpose, the values were transformed from RMS to PSD taking into account the Hanning window factor, the spectral resolution (Δf), and the squared RMS pressure. As identified by other authors, the VK spectrum has a small problem in the high-frequency region (dissipation range) where the spectrum changes from a $-5/3$ slope to an exponential decay [22]. A revision can be made using Pope's correction [46] so that the dissipation range is obtained by multiplying the energy spectrum mentioned above by a function of the form
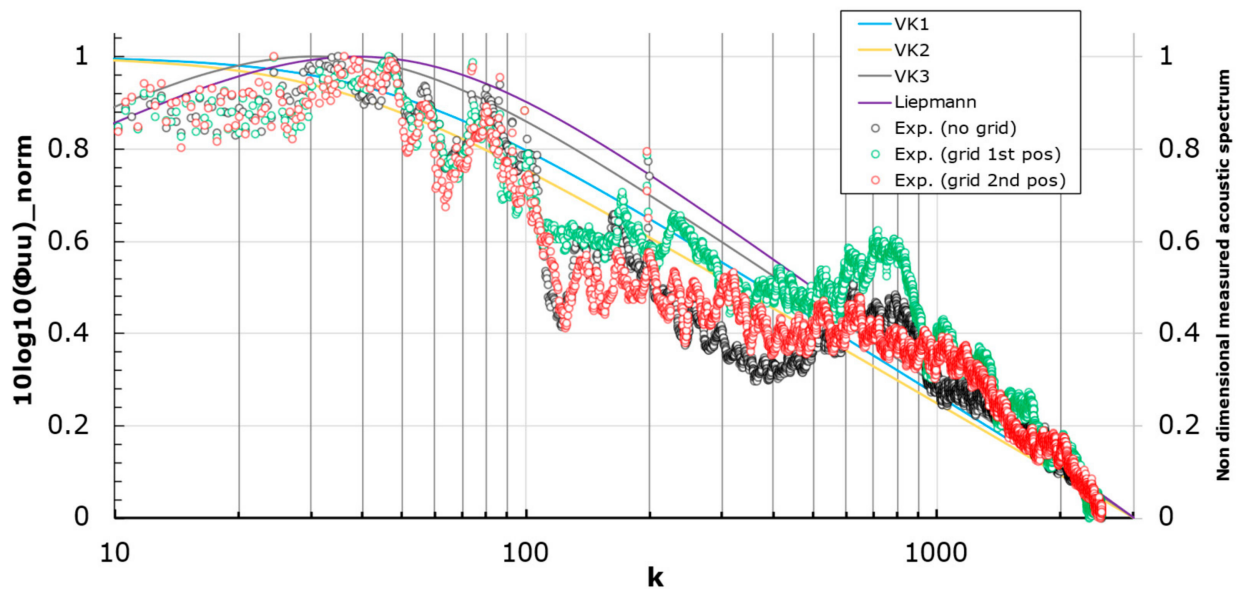
$$
f_\eta(k, \eta)_{Pope} = \exp\left(-B(k\eta)^n\right)
\tag{5}
$$

where *B* and *n* can have different values depending on the formulations, for example 2.1 and 1 or 9/4 and 2 [46]; the smallest length scale (η) is calculated using

$$\eta = \left(\frac{v^2}{15 \frac{\overline{u^2}}{\left(2\lambda_f\right)^2}} \right)^{\frac{1}{4}} \tag{6}$$
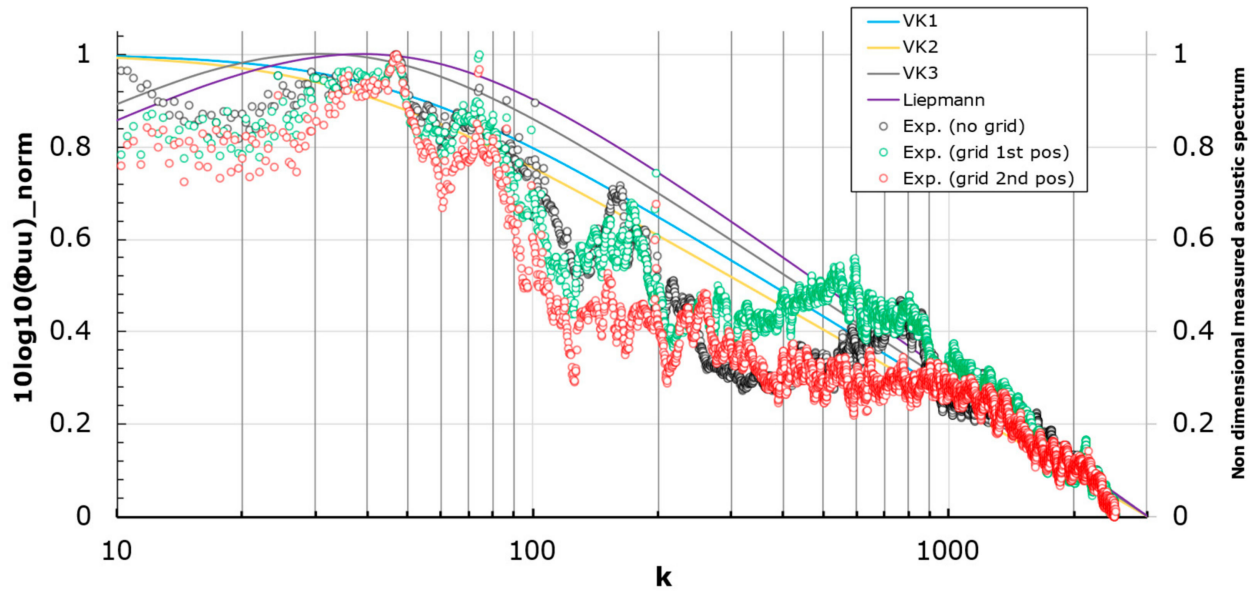

(**a**)

(**b**)

Figure 9. Several spectra formulations vs. experimental data: (**a**) $10°$ relative to the flow axis; (**b**) $90°$ relative to the flow axis; the VK1, VK2, VK3 and Liepmann spectra plotted using the equations from (in order) [58–61].

The Liepmann spectrum, on the other hand, seems to follow the experimental data quite well [22].

Placing the grid at the first position (more than 500 mm upstream of the vanes) did not lead to the production of high-intensity turbulence so that the spectra recorded in Figure 10 are not close to those obtained with the turbulence source placed closer to the nozzle outlet. However, a decrease in the sound pressure level over the range of 2–5 kHz (recorded by both microphones) is observed for the vanes with serrations at the trailing edge. This reduction (even of 15 dB on some frequencies) may be a particularity of the directivity of such solutions and should be investigated further. Overall, it was observed that to maintain the fluctuating character of the flow, the turbulence-generating mechanism should be placed close to the vane due to the vortices arising dissipating very quickly in the fluid mass.
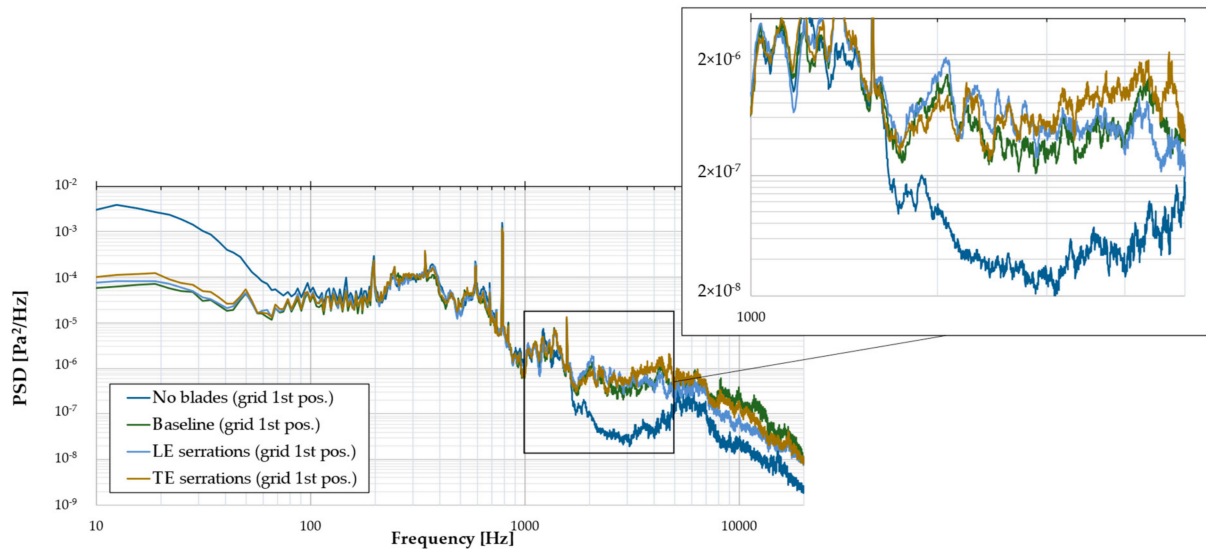
(**a**)
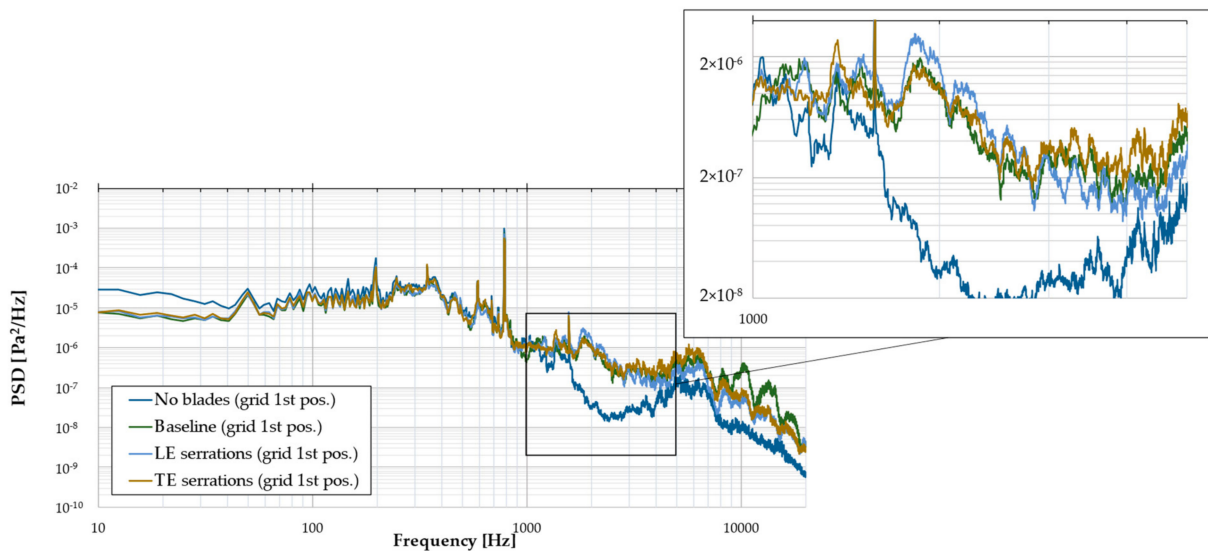
(**b**)

Figure 10. Interaction noise (turbulence grid at 1st position): (**a**) 0–20 kHz spectrum + detail on the frequency range of interest (multiples of BPF)—Microphone 1 (10 degrees to the longitudinal axis); (**b**) 0–20 kHz spectrum + detail on the frequency range of interest (multiples of BPF)—Microphone 2 (⊥ to the longitudinal axis).

Presenting the OASPL (overall sound pressure level) is preferred as it provides a global measure of sound intensity in dB, representing the total acoustic pressure. In contrast, PSD (Power Spectral Density) only examines power distribution across frequencies, without accounting for the cumulative acoustic effect. A comparative representation of the global sound pressure levels, derived from the corresponding spectra, is shown in Figure 11. The tonal components, including the first tone at 780 Hz (Figure 10), have been filtered.
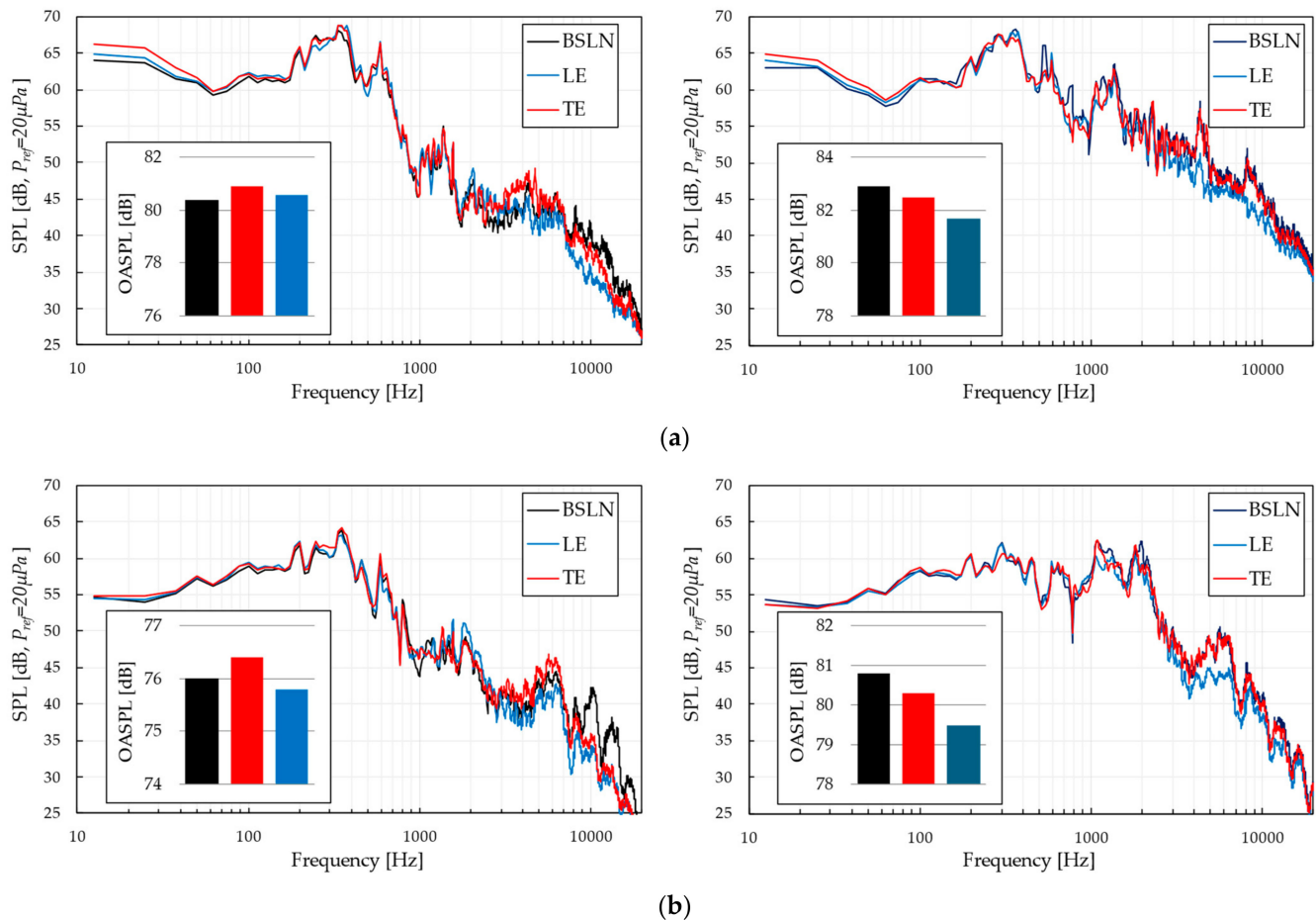

Figure 11. Sound pressure level spectra (left—turbulence grid at 1st position; right—turbulence grid at 2nd position): (**a**) 10 degrees to the longitudinal axis; (**b**) ⊥ to the longitudinal axis.

It can be observed that positioning the grid at the first position alters the global values (this was also evident numerically in the power spectra, where the interaction was not well represented). In contrast, a reduction of approximately 1.5 dB (OASPL) was observed for the grid–LE interaction noise in both measurement directions. The noise at the trailing edge was less attenuated; however, such serrations had a similar impact across the entire frequency range. The optimal operational range for the serrations placed at the leading edge, in the tested combinations, appears to be in the mid-frequency range (2000–5000 Hz). The difference in global levels observed in Figure 11 may be a characteristic of directivity, which will be further addressed in the future through the use of microphone arrays.

4. Conclusions

Good agreement was found between the analytical non-dimensional spectra and the measured spectra for the two grid positions at frequencies above 500 Hz. The designed setup was shown to effectively generate turbulence in the first BPF range. This capability allowed for the identification of interaction noise between the turbulent jet and the classical vane, with SPL reductions observed (at least qualitatively) in the 1000–3000 Hz range, despite the lack of proper correlation between the serration pitch and turbulence length

scale. Globally, a positive influence of the serrations was also observed at high frequencies, with OASPL decreasing by up to 1.5 dB for a cascade configuration with three blades of 50 mm × 75 mm. Placing the grid too far in front of the blades leads to a faster dissipation of fluctuations due to viscosity, failing to capture the turbulent jet–blade interaction. Overall, such configurations resulted in even higher noise levels (+0.5 dB in OASPL for the serrations at the TE). The results can be refined by eliminating as many undesirable acoustic sources as possible (impeller noise, leak noise, casing vibration) by introducing mufflers and by laminating/limiting the flow on the section within the largest diameter by placing a mesh or silencing grids. Directivity measurements are mandatory for the upcoming tests.

Initial results have indicated that interaction noise becomes prominent when perturbations occur near the stator. Future tests will involve grids of varying sizes positioned downstream of the nozzle, but still in close proximity. Additionally, rods will be used to assess the behavior of airfoils at specific frequencies. Aerodynamic testing will be conducted on the test stand, utilizing specially designed areas for mounting force transducers. The experimental geometries will be complemented by numerical simulations to further elucidate the underlying mechanisms. Future efforts will also focus on identifying acoustic sources (on isolated blades) using an acoustic camera, as well as visualizing flow patterns with PIV or Schlieren techniques.

Nomenclature

f	frequency [Hz]
k	wave number [1/m]
k_e	wavenumber scale of the largest eddies [1/m]
p'	pressure fluctuation [N/m^2]
u'	velocity fluctuation [m/s]
B	constant [-]
$E(k)$	energy spectrum [(m/s)^2/Hz]
K	kinetic energy [m^2/s^2]
TI	turbulent intensity [-]
ς	function of λ[m]
λ, Λ	integral length scale [m]
η	the smallest length scale [m]
v	kinematic viscosity [m^2/s]
$\Phi_{uu}(k_x)$	von Kármán longitudinal one-dimensional turbulence spectrum [(m/s)^2/Hz]
Γ	gamma function [-]

References

1. Westley, R.; Lilley, G.M. *An Investigation of the Noise Field from a Small Jet and Methods for Its Reduction*; College of Aeronautics Report; Cranfield University: Bedford, UK, 1952.
2. Biedermann, T.M.; Czeckay, P.; Hintzen, N.; Kameier, F.; Paschereit, C.O. Applicability of Aeroacoustic Scaling Laws of Leading Edge Serrations for Rotating Applications. *Acoustics* **2020**, *2*, 579–594. [CrossRef]
3. Lee, H.M.; Lim, K.M.; Xie, J.; Lee, H.P. Experimental Study on the Half Flat Tip Serrated Trailing Edge for Stand Fan. *Arch. Acoust.* **2020**, *45*, 359–365. [CrossRef]
4. Becker, S.; Riedel, J.; Kaltenbacher, M.; Schoder, S.; Czwielong, F. On the fluid mechanical and acoustic mechanisms of serrated leading edges. In Proceedings of the FAN 2022—International Conference on Fan Noise, Aerodynamics, Applications and Systems, Senlis, Frankreich, 27–29 June 2022. [CrossRef]
5. Chen, L.; Yang, P.; Zhang, B.; Chen, L. Aerodynamic Enhancement of Vertical-Axis Wind Turbines Using Plain and Serrated Gurney Flaps. *Appl. Sci.* **2023**, *13*, 12643. [CrossRef]
6. Qaissi, K.; Elsayed, O.; Faqir, M.; Essadiqi, E. Aerodynamic Optimization of Trailing-Edge Serrations for a Wind Turbine Blade Using Taguchi Modified Additive Model. *Energies* **2023**, *16*, 1099. [CrossRef]
7. Tay, W.B.; Lu, Z.; Ramesh, S.S.; Khoo, B.C. Numerical Simulations of Serrated Propellers to Reduce Noise. In *Supercomputing Frontiers. SCFA 2020*; Panda, D., Ed.; Lecture Notes in Computer Science; Springer: Cham, Switzerland, 2020; Volume 12082. [CrossRef]
8. Lee, H.M.; Lu, Z.; Lim, K.M.; Xie, J.; Lee, H.P. Quieter propeller with serrated trailing edge. *Appl. Acoust.* **2019**, *146*, 227–236, ISSN 0003-682X. [CrossRef]
9. Tam, C.K.W.; Viswanathan, K.; Ahuja, K.K.; Panda, J. The sources of jet noise: Experimental evidence. *J. Fluid Mech.* **2008**, *615*, 253–292. [CrossRef]
10. Juknevicius, A.; Chong, T.P. On the leading edge noise and aerodynamics of thin aerofoil subjected to the straight and curved serrations. *J. Sound Vib.* **2018**, *425*, 2018. [CrossRef]
11. Rego, L.; Avallone, F.; Ragni, D.; Casalino, D. On the mechanisms of jet-installation noise reduction with flow-permeable trailing edges. *J. Sound Vib.* **2021**, *520*, 2022. [CrossRef]
12. Vieira, A.E.; von den Hoff, B.; Snellen, M.; Simons, D.G. Comparison of Semi-Empirical Noise Models with Flyover Measurements of Operating Aircraft. *J. Aircr.* **2022**, *59*, 1574–1587. [CrossRef]
13. Henderson, B.S.; Huff, D.L.; Berton, J.J. Jet Noise Prediction Comparisons with Scale Model Tests and Learjet Flyover Data. Book Chapter. In Proceedings of the 25th AIAA/CEAS Aeroacoustics Conference, Delft, The Netherlands, 20–23 May 2019. [CrossRef]
14. Al Tlua, B. Experimental Wind Tunnel Testing and Numerical Optimization Studies for Airfoil Trailing Edge Noise Reduction. Ph.D. Thesis, Carleton University, Ottawa, ON, Canada, 2021. [CrossRef]
15. Lewis, D.; de Laborderie, J.; Sanjosé, M.; Moreau, S.; Jacob, M.C.; Masson, V. Parametric study on state-of-the-art analytical models for fan broadband interaction noise predictions. *J. Sound Vib.* **2021**, *514*, 116423. [CrossRef]
16. Raposo, H.; Azarpeyvand, M. Turbulence ingestion noise generation in rotating blades. *J. Fluid Mech.* **2024**, *980*, A53. [CrossRef]
17. Zorumski, W.E.; Weir, D.S. Empirical Source Noise Prediction Method with Application to Subsonic Coaxial jet Mixing Noise, NASA TP 2084 c.1. Available online: https://ntrs.nasa.gov/citations/19830007878 (accessed on 15 October 2024).
18. Powell, A. *On the Generation of Noise by Turbulent Jets*; The American Society of Mechanical Engineers: New York, NY, USA, 1959; AD-A286 649. [CrossRef]
19. Guérin, S.; Kissner, C.; Seeler, P.; Blázquez, R.; Carrasco Laraña, P.; de Laborderie, H.; Lewis, D.; Chaitanya, P.; Polacsek, C.; Thisse, J. ACAT1 Benchmark of RANS-Informed Analytical Methods for Fan Broadband Noise Prediction: Part II—Influence of the Acoustic Models. *Acoustics* **2020**, *2*, 617–649. [CrossRef]
20. Seoud, R.E.; Vassilicos, J.C. Dissipation and decay of fractal-generated turbulence. *Phys. Fluids* **2007**, *19*, 105108. [CrossRef]
21. Trevor; Stout, A.; Gee, K.L.; Neilsen, T.B.; Wall, A.T.; James, M.M. Intensity analysis of the dominant frequencies of military jet aircraft noise. *Proc. Mtgs. Acoust.* **2013**, *20*, 040010. [CrossRef]
22. Polacsek, C.; Buszyk, M.; Barrier, R.; Clair, V.; Salze, E. Aeroacoustic performances of a low-noise airfoil cascade with serrated leading edges: Predictions and measurements. In Proceedings of the ICAS 2022, Stockholm, Sweden, 4–9 September 2022. hal-03938107.
23. Abbas, M.; Riggins, D.W. Analysis of Energy Utilization and Losses for Jet-Propelled Vehicles. *Aerospace* **2021**, *8*, 342. [CrossRef]
24. Rota, G.F.; Monti, A.; Rosti, M.E.; Quadrio, M. Saving energy in turbulent flows with unsteady pumping. *Sci. Rep.* **2023**, *13*, 1299. [CrossRef]
25. Mahmoudi, M.; Banihashemi, M.A. Turbulence effect on total mechanical energy budget and energy loss of turbulent flows with different hydraulic regimes in open-channel transitions. *ISH J. Hydraul. Eng.* **2023**, *30*, 367–371. [CrossRef]
26. Wilson, D.K. Three-Dimensional Correlation and Spectral Functions for Turbulent Velocities in Homogeneous and Surface-Blocked Boundary Layers, Army Research Lab Adelphi MD, ADA327709. Available online: https://apps.dtic.mil/sti/citations/tr/ADA327709 (accessed on 15 October 2024).
27. Ragni, D.; Fiscaletti, D.; Baars, W.J. Jet noise predictions by time marching of single-snapshot tomographic PIV fields. *Exp. Fluids* **2022**, *63*, 84. [CrossRef]
28. da Soghe, R.; Innocenti, L.; Andreini, A.; Poncet, S. Numerical Benchmark of Turbulence modelling in Gas Turbine Rotor-Stator System. In Proceedings of the ASME TURBO EXPO 2010: Power for Land, Sea & Air (GT2010), Glasgow, UK, 14–18 June 2010. Available online: https://hal.science/hal-00679123 (accessed on 15 October 2024).

29. Fiore, M.; Gourdain, N. Reynolds, Mach, and Freestream Turbulence Effects on the Flow in a Low-Pressure Turbine. *J. Turbomach.* **2021**, *143*, 101009–1010022. Available online: https://hal.science/hal-03238795 (accessed on 15 October 2024). [CrossRef]

30. Michel, U.; Ahuja, K.K. On the Scaling of Jet Noise with Helmholtz Number Close to the Jet Axis. In Proceedings of the 20th AIAA/CEAS Aeroacoustics Conference, Atlanta, GA, USA, 16–20 June 2014. [CrossRef]

31. Rajeshwaran, M.S.; Kushari, A. Experimental Study on the Flow Past Sinusoidal Leading Edge Serrations in a Compressor Cascade. In Proceedings of the ASME 2015 Gas Turbine India Conference, Hyderabad, India, 2–3 December 2015; V001T01A017. [CrossRef]

32. Geiger, D. Comparative Analysis of Serrated Trailing Edge Designs on Idealized Aircraft Engine Fan Blades for Noise Reduction., Virginia Tech. 2005. Available online: https://vtechworks.lib.vt.edu/items/6caef5e2-88ac-4037-b95c-7f5bfa4fbc51 (accessed on 15 October 2024).

33. Lacagnina, G.; Chaitanya, P.; Kim, J.-H.; Berk, T.; Joseph, P.; Choi, K.-S.; Ganapathisubramani, B.; Hasheminejad, S.M.; Chong, T.P.; Stalnov, O.; et al. Leading edge serrations for the reduction of aerofoil self-noise at low angle of attack, pre-stall and post-stall conditions. *Int. J. Aeroacoustics* **2021**, *20*, 130–156. [CrossRef]

34. Salehian, S.; Mankbadi, R. Jet Noise in Airframe Integration and Shielding. *Appl. Sci.* **2020**, *10*, 511. [CrossRef]

35. Grasso, G.; Jaiswal, P.; Wu, H.; Moreau, S.; Roger, M. Analytical models of the wall-pressure spectrum under a turbulent boundary layer with adverse pressure gradient. *J. Fluid Mech.* **2019**, *877*, 1007–1062. Available online: https://hal.science/hal-03158378 (accessed on 15 October 2024). [CrossRef]

36. Shahzad, H.; Hickel, S.; Modesti, D. Permeability and Turbulence Over Perforated Plates. *Flow Turbul. Combust* **2022**, *109*, 1241–1254. [CrossRef]

37. Vemulapalli, S.; Venkata, S.K. Parametric analysis of orifice plates on measurement of flow: A review. *Ain Shams Eng. J.* **2022**, *13*, 101639. [CrossRef]

38. Pramiyanti, Y.; Seri, S.M.; Sapit, A. Incompressible Turbulent Swirling Flow through Circle Grid Perforated Plate. *J. Complex Flow* **2020**, *2*, 11–16.

39. Larssen, J.V.; Devenport, W.J. On the generation of large-scale homogeneous turbulence. *Exp. Fluids* **2011**, *50*, 1207–1223. [CrossRef]

40. Greschner, B.; Peth, S.; Moon, Y.J.; Seo, J.H.; Jacob, M.C.; Thiele, F. Three-dimensional predictions of the rod wake-airfoil interaction noise by hybrid methods. In Proceedings of the 14th International Congress on Sound and Vibration, ICSV 2007, Cairns, Australia, 9–12 July 2007; Volume 2, p. 1599–1610.

41. Teruna, C.; Ragni, D.; Avallone, F.; Casalino, D. A rod-linear cascade model for emulating rotor-stator interaction noise in turbofans: A numerical study. *Aerosp. Sci. Technol.* **2019**, *90*, 275–288. [CrossRef]

42. Sreenivasan, A.A.R.; Iyer, B.K. Enhanced wall turbulence model for flow over cylinder at high Reynolds number. *AIP Adv.* **2019**, *9*, 095012. [CrossRef]

43. Prince, S.A.; Khodagolian, V.; Gaind, R. An experimental study of a pulsed air jet and an acoustic synthetic jet on a low speed turbulent boundary layer. In Proceedings of the 28th Congress of the International Council of the Aeronautical Sciences ICAS 2012, Brisbane, Australia, 23–28 September 2012; Volume 2, pp. 1005–1014.

44. Blake, J.D.; Sescu, A.; Thompson, D.; Hattori, Y. A Coupled LES-Synthetic Turbulence Method for Jet Noise Prediction. *Aerospace* **2022**, *9*, 171. [CrossRef]

45. Dieste, M.; Gabard, G. Broadband Interaction Noise Simulations Using Synthetic Turbulence. In Proceedings of the Sixteenth International Congress on Sound and Vibration, Krakow, Poland, 5–9 July 2009.

46. Dos Santos, F.L.; Botero, L.; Venner, C.; de Santana, L.D. Modelling the Dissipation Range of von Kármán Turbulence Spectrum. In Proceedings of the AIAA AVIATION 2021 FORUM, Virtual Event, 2–6 August 2021. [CrossRef]

47. Philips, C.; Bandyopadhyay, R.; McComas, D.J. Taylor Microscale and Effective Reynolds Number near the Sun from PSP. *Astrophys. J.* **2022**, *933*, 33. [CrossRef]

48. Wang, B.; Manhart, M. Two-phase micro- and macro-time scales in particle-laden turbulent channel flows. *Acta Mech. Sin.* **2012**, *28*, 595–604. [CrossRef]

49. Li, D.; Salesky, S.T.; Banerjee, T. Connections between the Ozmidov scale and mean velocity profile in stably stratified atmospheric surface layers. *J. Fluid Mech.* **2016**, *797*, R3. [CrossRef]

50. Wang, G.-H.; Clemens, N.T.; Barlow, R.S.; Varghese, P.L. A system model for assessing scalar dissipation measurement accuracy in turbulent flows. *Meas. Sci. Technol.* **2007**, *18*, 1287–1303. [CrossRef]

51. Essa, K.S.M. Estimation of MONIN-OBUKHOV length using richardson and bulk richardson number. In Proceedings of the Second Conference on Nuclear and Particle Physics (NUPPAC-99), Cairo, Egypt, 13–17 November 1999; p. 711.

52. Dong, S.; Huang, Y.; Yuan, X.; Lozano-Durán, A. The coherent structure of the kinetic energy transfer in shear turbulence. *J. Fluid Mech.* **2020**, *892*, A22. [CrossRef]

53. Kim, S.; Jung, H.; Kong, M.J.; Lee, D.K.; An, Y.-K. In-Situ Data-Driven Buffeting Response Analysis of a Cable-Stayed Bridge. *Sensors* **2019**, *19*, 3048. [CrossRef]

54. Palani, S.; Paruchuri, C.C.; Joseph, P.; Karabasov, S.A.; Markesteijn, A.; Abid, H.; Chong, T.P.; Utyuzhnikov, S. Modified TNO-Blake model for aerofoil surface pressure prediction with canopies. AIAA 2023-3203. In Proceedings of the AIAA AVIATION 2023 Forum, San Diego, CA, USA, 12–16 June 2023.

55. Smith, E.G.; Sowers, H.D. *Cascade Tests of Serrated Leading Edge Blading at High Subsonic Speeds*; NASA: Washington, DC, USA, 1974; NASA CR-2472.

56. Goldstein, M.E. The 90 Deg Acoustic Spectrum of a High Speed Air Jet, NASA E-14396. Available online: https://ntrs.nasa.gov/citations/20050196696 (accessed on 15 October 2024).

57. McLaughlin, D.; Kno, C.W.; Papamoschou, D. Experiments on the Effect of Ground Reflections on Supersonic Jet Noise. In Proceedings of the 46th AIAA Aerospace Sciences Meeting and Exhibit, Reno, NV, USA, 7–10 January 2008. [CrossRef]

58. Yasir, A.-O. Effect of Leading Edge Blowing for Aero Foil Subjected to Laminar and Turbulent Inflows. Ph.D. Thesis, Brunel University London, London, UK, 2020.

59. Gruber, M. Airfoil Noise Reduction by Edge Treatments. Ph.D. Thesis, University of Southampton, Southampton, UK, 2012.

60. Lyu, B.; Azarpeyvand, M. On the noise prediction for serrated leading edges. *J. Fluid Mech.* **2017**, *826*, 205–234. [CrossRef]

61. Lyu, B.; Ayton, L.J. Rapid Noise Prediction Models for Serrated Leading and Trailing Edges. *J. Sound Vib.* **2020**, *469*, 115136. [CrossRef]